

Supplementary Information

Effective Intrinsic Charge Carrier Correction for Interface Charge Transfer Modeling of Perovskite Solar Cells in Dark Conditions [★]

J. A. Jiménez-Tejada^{a,*}, M. García-Rosell^a, O. Almora^c, P. López-Varo^b

^a*Departamento de Electrónica y Tecnología de Computadores, CITIC-UGR, Universidad de Granada, Granada 18071, Spain*

^b*Institut Photovoltaïque d'Île-de-France 30 RD 128, 91120, Palaiseau, France*

^c*Department of Electrical Electronic and Automatic Engineering, Universitat Rovira i Virgili, Tarragona 43007, Spain*

Contents

S1 Reference structure	2
S2 Bulk recombination in the perovskite	2
S3 Physical validity of interface recombination models	4
S4 Effect of B_S and $\tau_n(= \tau_p)$ in Models 1 and 2	6
S5 Interface recombination in only one interface.	6
S6 Effect of the thickness δ in Models 3 and 4	10
S7 Effect of the ion concentration in Models 3 and 4	12
S8 Effect of the built-in voltage (band alignment at the interfaces) in Models 3 and 4	13
S9 Effect of the shunt resistance	16

[★]The authors acknowledge support from the project PID2022-139586NB-44 funded by MCIN/AEI/10.13039/501100011033 and by European Union NextGenerationEU/PRTR.

*Corresponding author.

Email addresses: tejada@ugr.es (J. A. Jiménez-Tejada), mgar3705@gmail.com (M. García-Rosell), osbel.almora@urv.cat (O. Almora), pilar.lopez-varo@ipvf.fr (P. López-Varo)

Parameters used in the numerical simulations

Name	Symbol	Unit	Value		
Unit charge	q	C	1.602×10^{-19}		
Vacuum permittivity	ϵ_0	F/cm	8.854×10^{-14}		
Density of states	$N_{C,V}$	cm^{-3}	10^{20}		
			HTL	Perovskite	ETL
Dielectric relative permittivity	ϵ_r	-	3	26	20
Electron mobility	μ_n	$\text{cm}^2/(\text{Vs})$	10^{-4}	10	1
Hole mobility	μ_p	$\text{cm}^2/(\text{Vs})$	10^{-4}	10	1
Bandgap	E_g	eV	3	1.6	3
Acceptor concentration	N_A	cm^{-3}	10^{17}	10^{17}	-
Donor concentration	N_D	cm^{-3}	-	-	10^{18}
Mobile ion concentration	N_{ion}	cm^{-3}	0	5×10^{17}	0
Generation rate of electron/hole pairs	G_0	$\text{cm}^{-3}\text{s}^{-1}$	-	0	-
Bulk recombination coefficient	B_B	cm^3s^{-1}	-	5×10^{-11}	-
Semiconductor layer length	L	nm	60	220	20
Discontinuity of the conduction band	ΔE_C	eV	1.8		0.4
Interface recombination coefficient	B_S	cm^3s^{-1}	-	10^{-6} (Model 1)	-
			-	10^{-14} (Model 3)	-
Interface trapping time constants	$\tau_n = \tau_p$	s	-	10^{-3} (Models 2 and 4)	-

Table S1: Values of the parameters used in the numerical simulations.

S1. Reference structure

A PSC is used as a reference for comparison with different other structures in the main text. This structure is simulated assuming bulk recombination mechanisms ($R = R_B \neq 0$) with a bulk recombination coefficient $B_B = 5 \times 10^{-11} \text{ cm}^3 \text{ s}^{-1}$, mobile cations and anions with average concentration $N_{ion} = 5 \times 10^{17} \text{ cm}^{-3}$, and neglecting the interface recombination mechanisms ($R_S = 0$). The fast $J - V$ curves calculated in darkness are depicted in Fig. S1 (a)-(b). The actual distribution of ions is calculated at the beginning of each sweep: $V_{ap} = -1 \text{ V}$ for the reverse sweep (RS), and $V_{ap} = 1 \text{ V}$ for the forward sweep (FS) (Fig. S1(c) and (d), respectively).

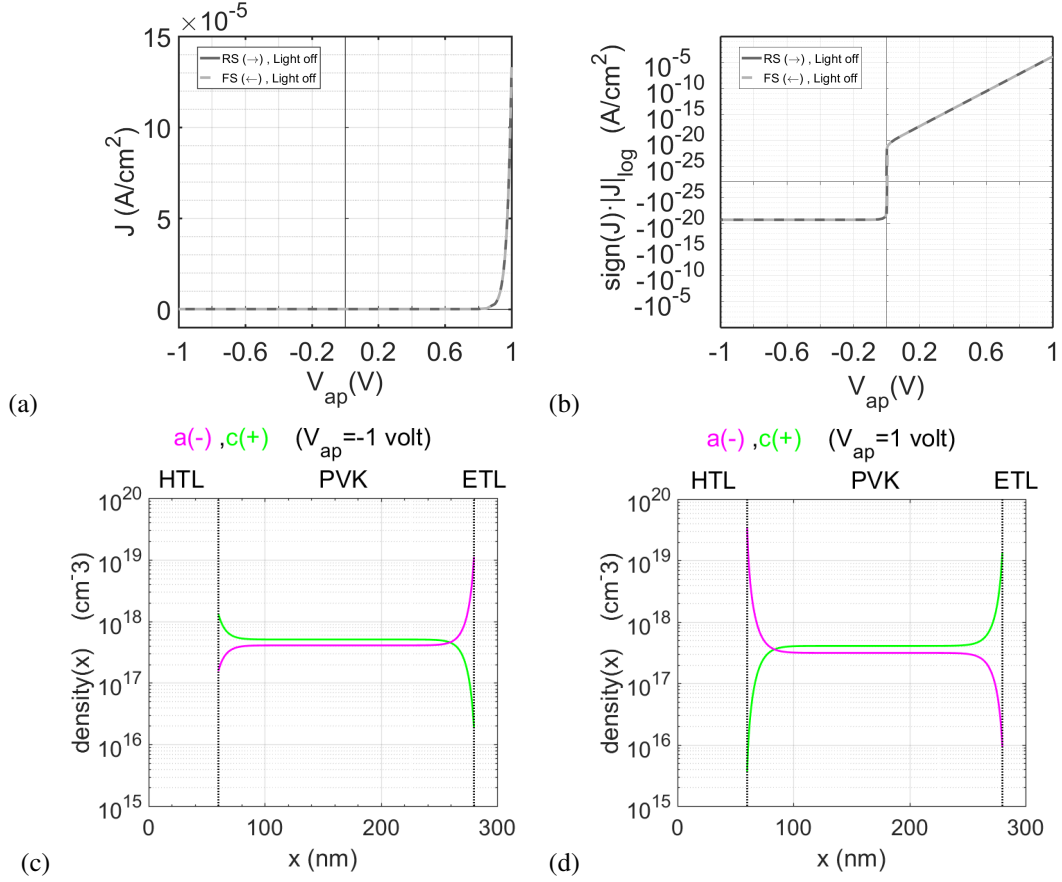


Figure S1: Fast $J - V$ curves calculated in darkness for a reference PSC with $B_B = 5 \times 10^{-11} \text{ cm}^3 \text{ s}^{-1}$, ion concentration $N_{ion} = 5 \times 10^{17} \text{ cm}^{-3}$ and neglecting interface recombination, depicted in (a) linear and (b) logarithmic scales for J . Distribution of ions during the fast (c) reverse and (d) forward sweeps of the $J - V$ curves.

S2. Bulk recombination in the perovskite

This study is made in order to check whether the bulk recombination alone can produce significant hysteresis in the $J - V$ curves. Three values of B_B in the range $[5 \times 10^{-11}, 5 \times 10^{-7}] \text{ cm}^3 \text{ s}^{-1}$ are used to calculate the fast $J - V$ curves

depicted in Fig. S2 for two values of the ion concentration, $N_{ion} = 0$ (Fig. S2(a)) and $N_{ion} = 5 \times 10^{17} \text{ cm}^{-3}$ (Fig. S2(b)). Recombination mechanisms at the interfaces are neglected in this test ($R_S = 0$). The lowest value $B_B = 5 \times 10^{-11} \text{ cm}^3 \text{ s}^{-1}$ corresponds to the reference sample (gray curves in Fig. S1).

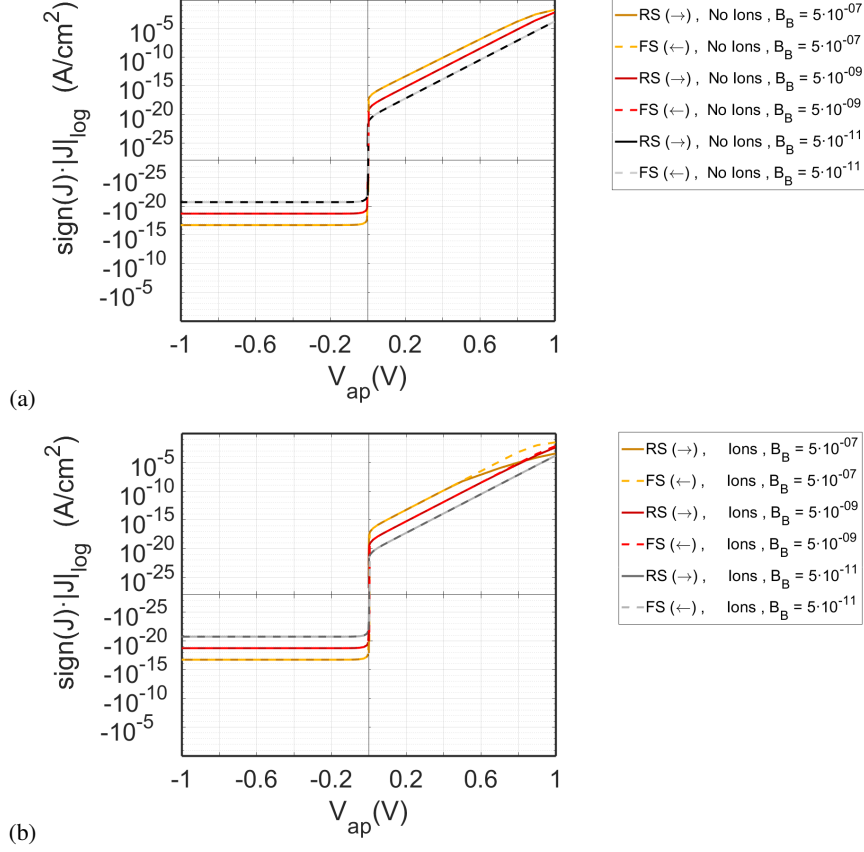


Figure S2: Fast $J - V$ curves calculated in darkness for a PSC, neglecting interface recombination, and considering bulk recombination with different values of B_B in $\text{cm}^3 \text{ s}^{-1}$ for two ion concentrations: (a) $N_{ion} = 0$ and (b) $N_{ion} = 5 \times 10^{17} \text{ cm}^{-3}$.

Figure S2 points out: (i) the current increases proportionally to the increment in B_B ; (ii) the linear trend observed in forward bias for the relation $\log(J) - V_{ap}$ is lost at high values of V_{ap} due to high injection effects; (iii) there is no hysteresis in the samples without ions (Fig. S2(a)); (iv) hysteresis is only seen in the samples with ions for high values of B_B ($B_B = 5 \times 10^{-7} \text{ cm}^3 \text{ s}^{-1}$) and $V_{ap} > 0.6 \text{ V}$ (yellow curves in Fig. S2(b)). This small hysteresis loop at high voltages is due to the fact that the current in the PSC at high voltage values depends on the bulk recombination coefficient and on the built-in potential. The higher the bulk recombination coefficient is, the higher the ion screening effect is, which produces an apparent modification of the built-in voltage. In the rest of values of the bias voltage no hysteresis is observed in the whole range of B_B . Throughout this work, the value of B_B is kept constant at $B_B = 5 \times 10^{-11} \text{ cm}^3 \text{ s}^{-1}$.

S3. Physical validity of interface recombination models

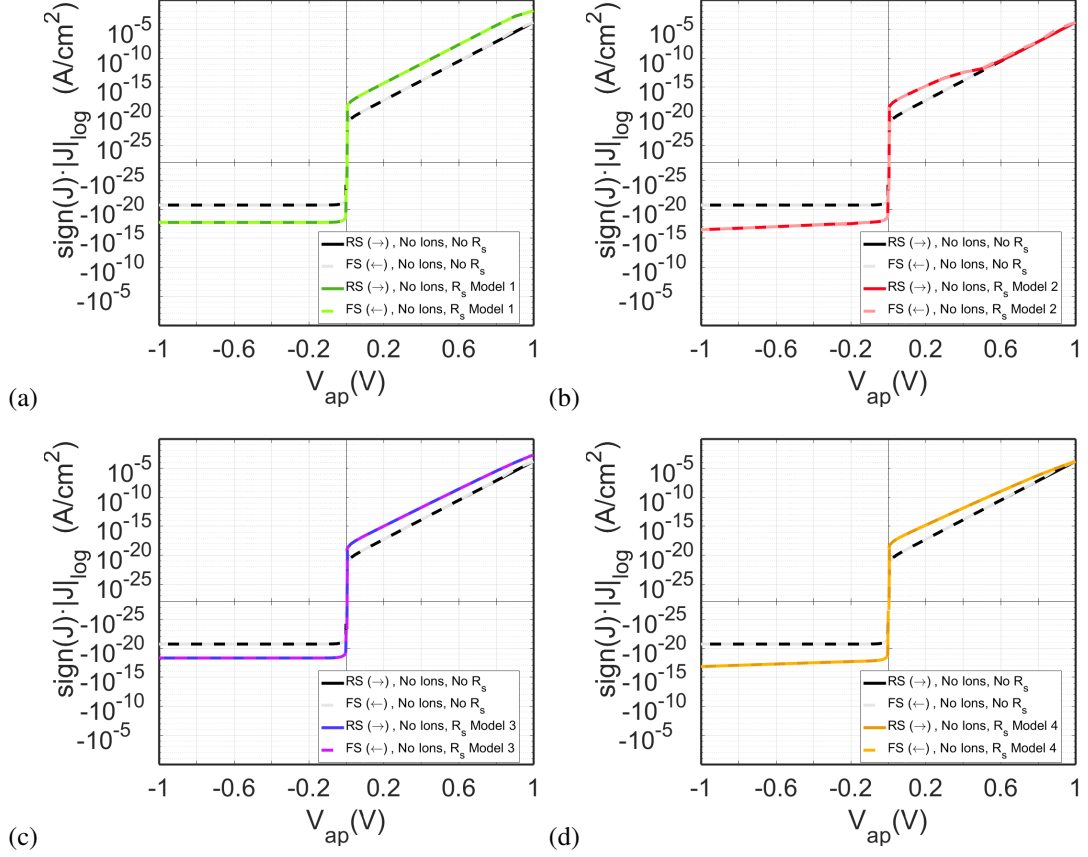


Figure S3: $J - V$ curves in darkness in a PSC without ions ($N_{ion} = 0$) calculated using, in both interfaces, different recombination models (a) Model 1 (green lines), (b) Model 2 (red lines), (c) Model 3 (blue lines), (d) Model 4 (yellow lines). As a reference, a $J - V$ curve for the same PSC, neglecting the interface recombination ($R_s = 0$), is represented in black and grey lines in all the figures.

In this section, we check the physical validity of the interface recombination Models 1–4. In addition, we present an example of an interface recombination model that reproduces the hysteresis loop around $V_{ap} = 0$ in $J - V$ curves in darkness but it can not be considered physically valid.

The necessary condition for a model to be physically valid is that in thermal equilibrium and $V_{ap} = 0$, the resulting current density in darkness must be $J = 0$. A graphical and quicker way to check this condition is by calculating and representing a $J - V$ curve in darkness for a PSC without ions.

Figure S3 shows $J - V$ curves calculated using recombination Models 1–4 in both interfaces in a PSC without ions. The values of the rest of the parameters are the same as in Fig. S1. Only for comparison reasons, a $J - V$ curve calculated for the same sample without ions and neglecting the recombination at the interfaces ($N_{ion} = 0$, $R_s = 0$) is represented in black and grey lines. As seen in the figure, every model fulfills the condition $J = 0$ at $V_{ap} = 0$.

Other secondary observations are: (i) there is no hysteresis without ions, as expected; (ii) the absolute value of the current is always greater when surface recombination is considered; and (iii) the shape of the three $J - V$ curves depend on the type of interface recombination model used in the simulation.

Other cross-recombination models can also be defined for the PSC interfaces with apparent satisfactory results in the fast $J - V$ curves, but they do not fulfill the condition $J = 0$ at $V_{ap} = 0$. An example is a modification of Model 3, when using local values for the concentrations of electrons, $n(x)$, and holes, $p(x)$, instead of the mean values, $\langle n(x) \rangle$ and $\langle p(x) \rangle$, respectively, used in (3)-(7). This model can be named Model 3.2, and is defined as:

$$R(x) = R_B(x) + W(x) \sum_{j=HTL/pvk}^{pvk/ETL} B_{S_j} \{n(x)p[x - 2(x - x_j)] - n_{i,eff}^2\} \quad (S1)$$

$$W(x) = \begin{cases} 1, & x \in [x_1, x_1 + \delta] \cup [x_2, x_2 + \delta] \\ 0, & \text{any other case} \end{cases}$$

where $x_{HTL/pvk} \equiv x_1$ and $x_{pvk/ETL} \equiv x_2$ in (S1).

Figure S4(a) shows in blue line a $J - V$ curve calculated in darkness and no ions using Model 3.2. It is compared with the reference curve for the PSC with no ions and no interface recombination (black and gray curve). Unlike the $J - V$ curves shown in Fig. S3, the blue curve in S4(a) does not fulfill the condition $J = 0$ at $V_{ap} = 0$. Note that $J = 0$ at $V_{ap} = -0.0375$ V. This model must be ignored, despite the fast $J - V$ curves calculated in a PSC with ions in darkness (blue lines in Fig. S4(b)) are very similar to the ones calculated for Model 3 (blue lines in Fig. 4(c)).

More examples of physical inaccurate models can be obtained from the modification of Models 3 and 4 when the term ni_{eff}^2 is neglected in their respective expressions (7) and (9). In these cases, the condition $J = 0$ at $V_{ap} = 0$ neither fulfills, as seen in Figs. S5(a) and (c) (blue and brown lines, respectively). These models must be ignored despite $J - V$ curves with a loop around $V_{ap} = 0$ are obtained when ions are introduced (see Figs. S5(b) and (d)).

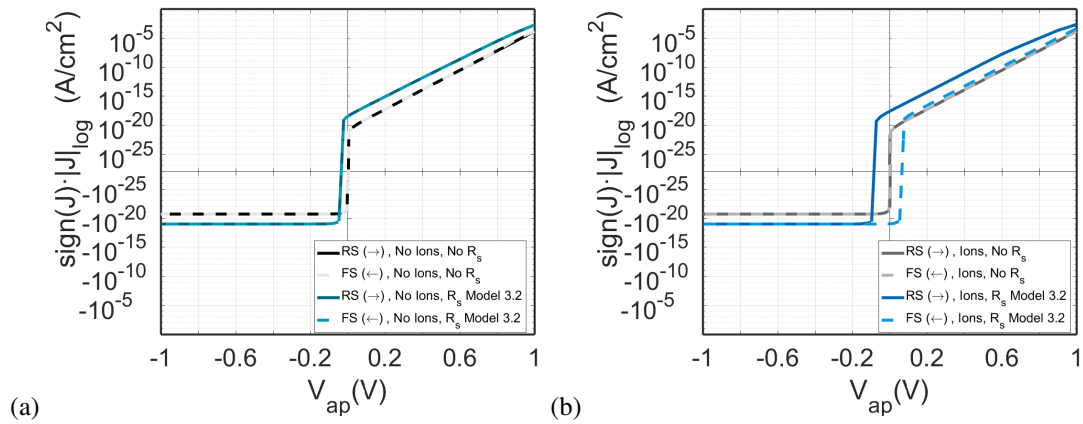


Figure S4: (a) $J - V$ curves in darkness in a PSC without ions ($N_{ion} = 0$) calculated using Model 3.2 (eq. S1) in both interfaces (blue lines). The $J - V$ curve for the reference PSC with no ions and no interface recombination is represented in black and gray. (b) Fast $J - V$ curves in darkness for the same PSC with ions ($N_{ion} = 5 \times 10^{17} \text{ cm}^{-3}$) and using Model 3.2 (blue lines), compared with a PSC with the same concentration of ions but no interface recombination (black and gray lines).

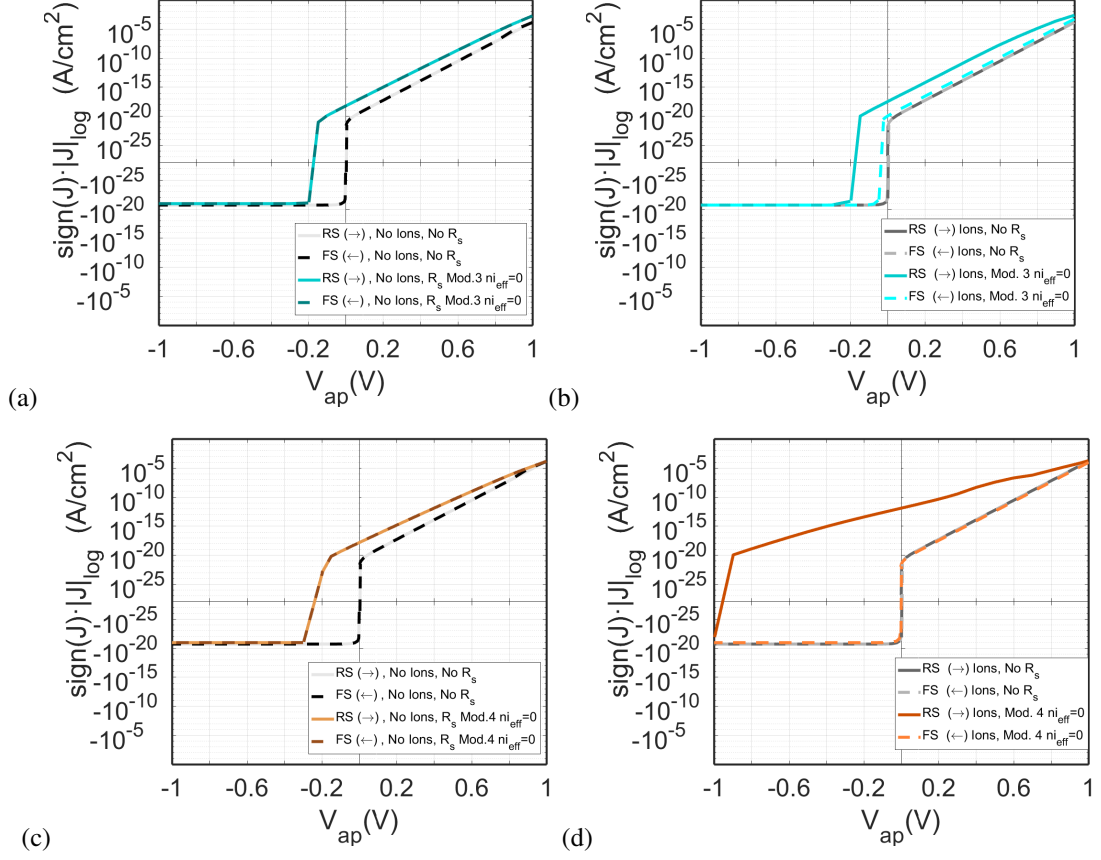


Figure S5: (a),(c): $J - V$ curves in darkness in a PSC without ions ($N_{ion} = 0$) calculated using Models 3 and 4 in both interfaces (blue and brown lines, respectively) when the term ni_{eff}^2 is neglected in (7) and (9), respectively. The $J - V$ curve for the reference PSC with no ions and no interface recombination is represented in black and gray. (b),(d): Fast $J - V$ curves in darkness for the same PSC when ions are included in the simulation ($N_{ion} = 5 \times 10^{17} \text{ cm}^{-3}$), compared with a PSC with the same concentration of ions but no interface recombination (gray lines).

S4. Effect of B_S and $\tau_n (= \tau_p)$ in Models 1 and 2

$J - V$ curves were calculated for different values of B_S ($[10^{-9}, 10^{-6}] \text{ cm}^3 \text{ s}^{-1}$) and $\tau_n = \tau_p$ ($[1 \text{ ms}, 1 \text{ s}]$) in the four models. Curves for Models 1 and 2 are represented here in Fig. S6 and curves for Model 3 and 4 are represented in the main text in Fig. 5.

S5. Interface recombination in only one interface.

Figure S7 shows fast $J - V$ curves in darkness calculated in a PSC with $N_{ion} = 5 \times 10^{17} \text{ cm}^{-3}$ and interface recombination R_S limited to only one of the two interfaces. The results are compared with the $J - V$ curves of the reference case, $N_{ion} = 5 \times 10^{17} \text{ cm}^{-3}$ and $R_S = 0$ (gray lines). The four models show a different behavior.

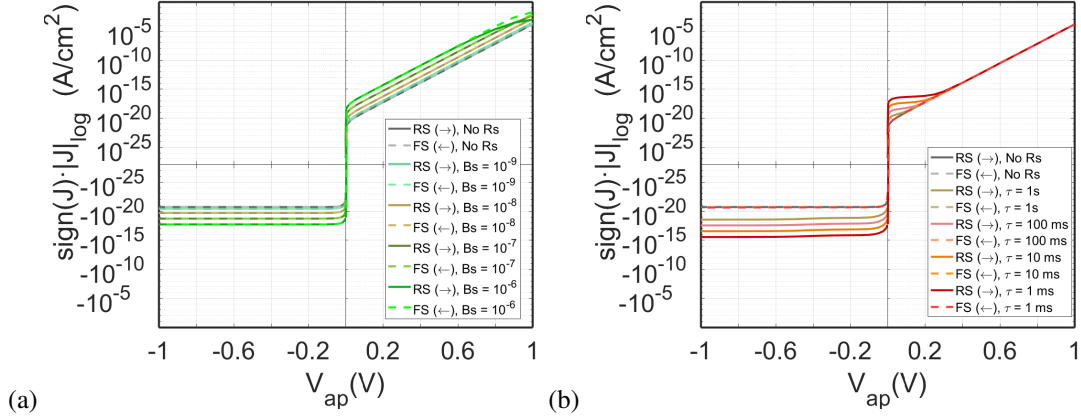


Figure S6: $J - V$ curves calculated using the interface recombination (a) Model 1 for different values of B_S ($[10^{-9}, 10^{-6}] \text{ cm}^3 \text{ s}^{-1}$) and (b) Model 2 for different values of $\tau_n = \tau_p$ ($[1 \text{ ms}, 1 \text{ s}]$). The reference case with no interface recombination is shown in gray lines.

Model 1

Figures S7(a) and (b) show the fast $J - V$ curves calculated with Model 1 applied to the HTL/pvk and pvk/ETL interfaces, respectively. Apparently, there is no difference between these curves and the ones represented in Fig. 4(a) when the model is applied to both interfaces. The current density calculated in Fig. S7(a) is slightly higher than the one represented in Fig. S7(b). The sum of both current densities represented in Figs. S7(a) and (b) coincides with the one represented in Fig. 4(a). The effects of each interface are additive. Each interface contributes with almost half of the current density to the total current. The high injection effects are lower in Figs. S7(a) and (b) than in Fig. 4(a) because the current is lower in the first two figures.

Model 2

Figures S7(c) and (d) show the fast $J - V$ curves calculated with Model 2 applied to the HTL/pvk and pvk/ETL interfaces, respectively. The forward sweeps are very similar in both Figs. S7(c) and (d) and in Fig. 4(b), in which Model 2 is applied to both interfaces. In the range $-0.6 < V_{ap} < 0.2$ V, the reverse sweep scan of Fig. S7(d) is different to the one represented in Fig. S7(c) but similar to the one represented in and Fig. 4(b). This means that the current density is controlled mainly by the pvk/ETL interface. Outside this range $-0.6 < V_{ap} < 0.2$ V in the reverse sweep, both interfaces contribute similarly with almost half of the total current density. The higher values of the doping concentration and the charge carrier mobility in the ETL in comparison to the HTL can explain this dissimilarity found in Figs. S7(c) and (d), in which the HTL/pvk interface seems to play a major role in contributing to the total current density.

Model 3

Figures S7(e) and (f) show the fast $J - V$ curves calculated with Model 3 applied to the HTL/pvk and pvk/ETL interfaces, respectively. At first glance, the $J - V$ curves seem very similar in both figures. However, significant

quantitative differences are observed.

(i) In the ranges $V_{ap} < -0.2$ V and $V_{ap} > 0.125$ V, the absolute value of the current density $|J|$ is one order of magnitude higher in Fig. S7(f) (interface recombination only in the pvk/ETL interface) than in Fig. S7(e) (interface recombination only in the HTL/pvk interface), and the value in Fig. S7(f) is very similar to the one obtained in Fig. 4(c)). Thus, the recombination effect in the pvk/ETL interface is the main contributor to the current density in this voltage range. This may be attributed to the higher values of the doping concentration and the charge carrier mobility in the ETL in comparison to the HTL, making the ETL more conductive than the HTL, and with more available free charges to recombine with.

(ii) In the range $-0.2 < V_{ap} < 0.125$ V, the current density increases when the voltage increases and changes its sign. In the forward sweep, the change of sign in J takes place at $V_{ap} = 0.125$ V in both Figs. S7(e) and (f) and also in Fig. 4(c). In the reverse sweep, the change of sign in J takes place at different values of V_{ap} : at $V_{ap} = -0.0375$ V in Fig. S7(e) and at $V_{ap} = -0.0175$ V in Figs. S7(f) and 4(c). The suppression of the interface recombination in the pvk/ETL interface makes the hysteresis loop slightly more symmetrical around $V_{ap} = 0$ V (Fig. S7(e)). Again, the higher values of the doping concentration and charge carrier mobility in the ETL and the fact that the perovskite is p-type doped may produce this asymmetrical loop around $V_{ap} = 0$ V. Many other combinations of doping concentration in the perovskite and CTLs should be necessary to verify this assessment.

Model 4

(i) Depending on the direction of the voltage sweep, one interface dominates over the other. In the reverse sweep and in the ranges $V_{ap} < -0.2$ V and $V_{ap} > 0$ V, $|J|$ is greater in Fig. S7(g) than in S7(h) and its value in Fig. S7(g) is similar to the one obtained in Fig. 4(d). In the forward sweep and in the range $V_{ap} < -0.2$ V, $|J|$ is greater in Fig. S7(h) than in S7(g) and its value in Fig. S7(h) is similar to the one obtained in Fig. 4(d); while in the range $V_{ap} > 0.125$ V, $|J|$ is the same in Figs. S7(h) and (g).

(ii) Like in Model 3, the suppression of the interface recombination in the pvk/ETL interface makes the hysteresis loop slightly more symmetrical around $V_{ap} = 0$ V (Fig. S7(g)). Again, the higher values of the doping concentration and charge carrier mobility in the ETL and the fact that the perovskite is p-type doped may produce this asymmetrical loop around $V_{ap} = 0$ V when the pvk/ETL interface is considered. Many other combinations of doping concentration in the perovskite and CTLs should be necessary to verify this assessment.

From the analysis of the curves in Fig. S7, only Model 3 and Model 4 lead to a significant hysteresis around $V_{ap} = 0$ V. This result is independent of applying any of these two models to only one interface (Fig. S7) or both interfaces (Fig. 4).

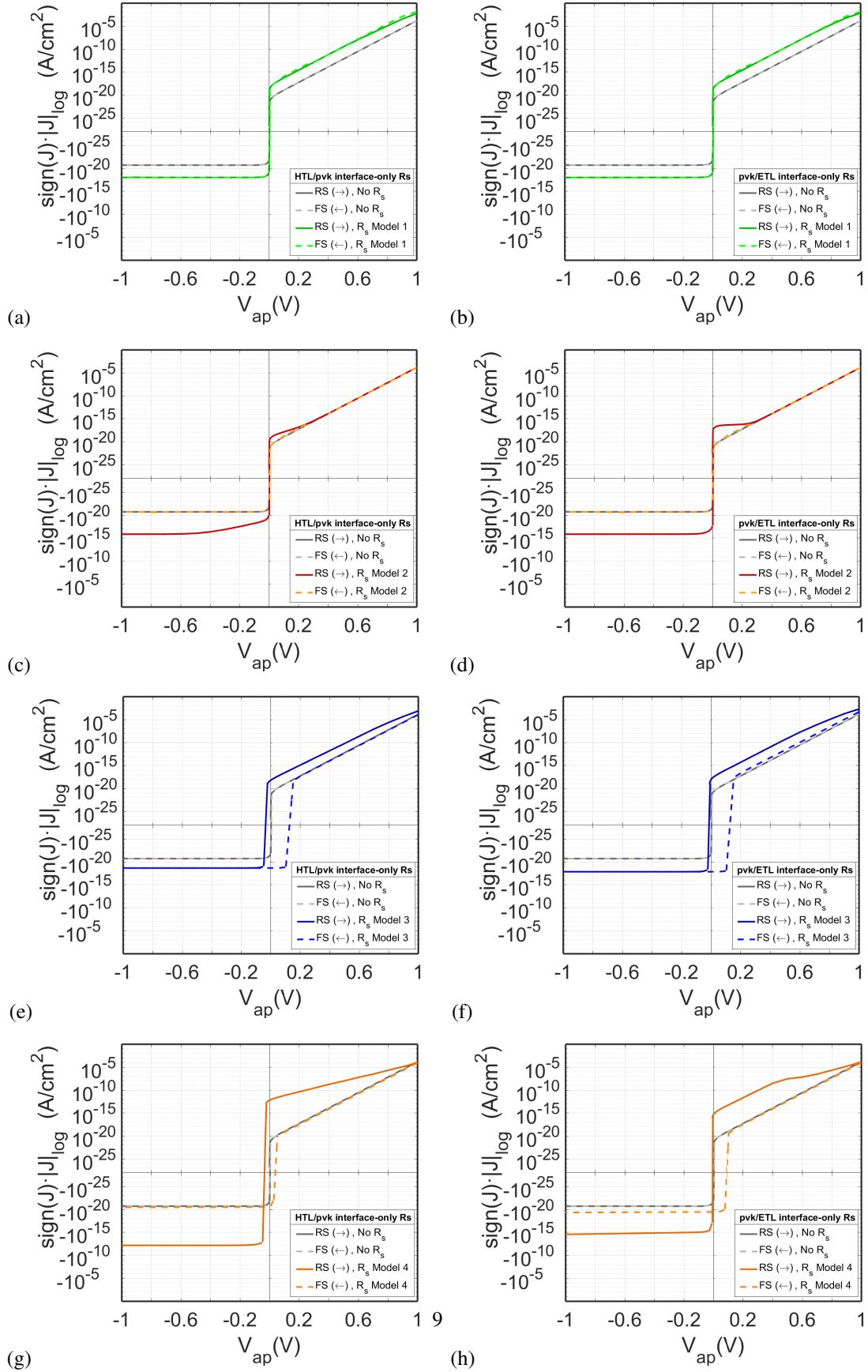


Figure S7: Fast $J - V$ curves calculated with $N_{ion} = 5 \times 10^{17} \text{ cm}^{-3}$ and interface recombination R_s considered in only one of the two interfaces: (a),(c),(e) HTL/pvk interface; and (b),(d),(f) pvk/ETL interface. (a), (b) Model 1; (c), (d) Model 2; (e), (f) Model 3; and (g), (h) Model 4. The curves for the reference case, $N_{ion} = 5 \times 10^{17} \text{ cm}^{-3}$ and $R_s = 0$, are depicted with gray lines.

S6. Effect of the thickness δ in Models 3 and 4

Figures S8 and S9 show a semi-logarithmic representation of fast $J - V$ curves evaluated using the interface recombination Models 3 and 4, respectively, applied in both interfaces for different values of the thickness δ of the effective layer in which the recombination model for R_S is computed ($\delta \in [0, 5]$ nm).

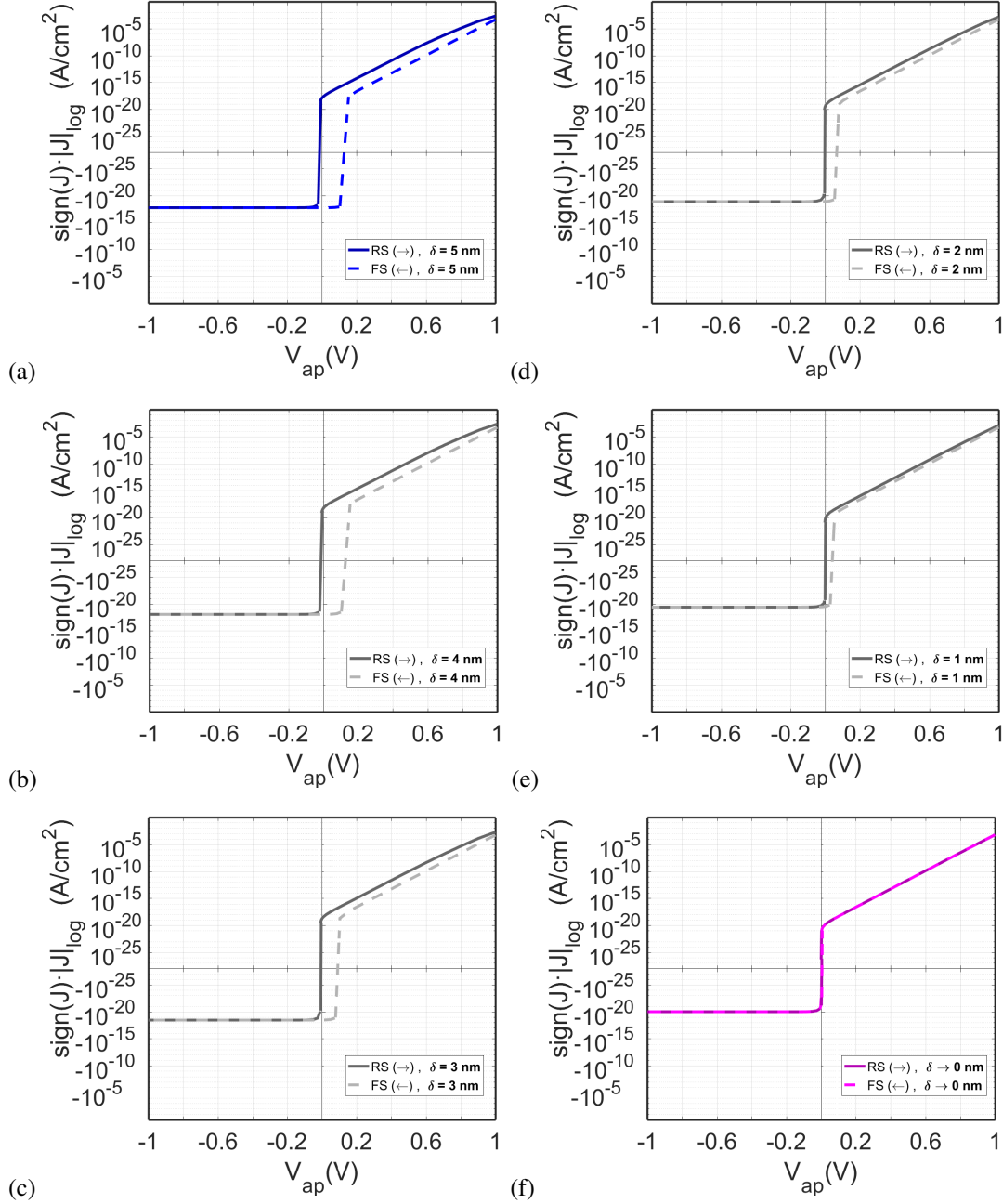


Figure S8: $J - V$ curves calculated using the interface recombination Model 3 with $N_{\text{ion}} = 5 \times 10^{17} \text{ cm}^{-3}$ and (a) $\delta = 5$ nm; (b) $\delta = 4$ nm; (c) $\delta = 3$ nm; (d) $\delta = 2$ nm; (e) $\delta = 1$ nm; and (f) limit case $\delta \rightarrow 0$ nm, evaluated using boundary conditions for the pvk/CTL interfaces (10) and (11).

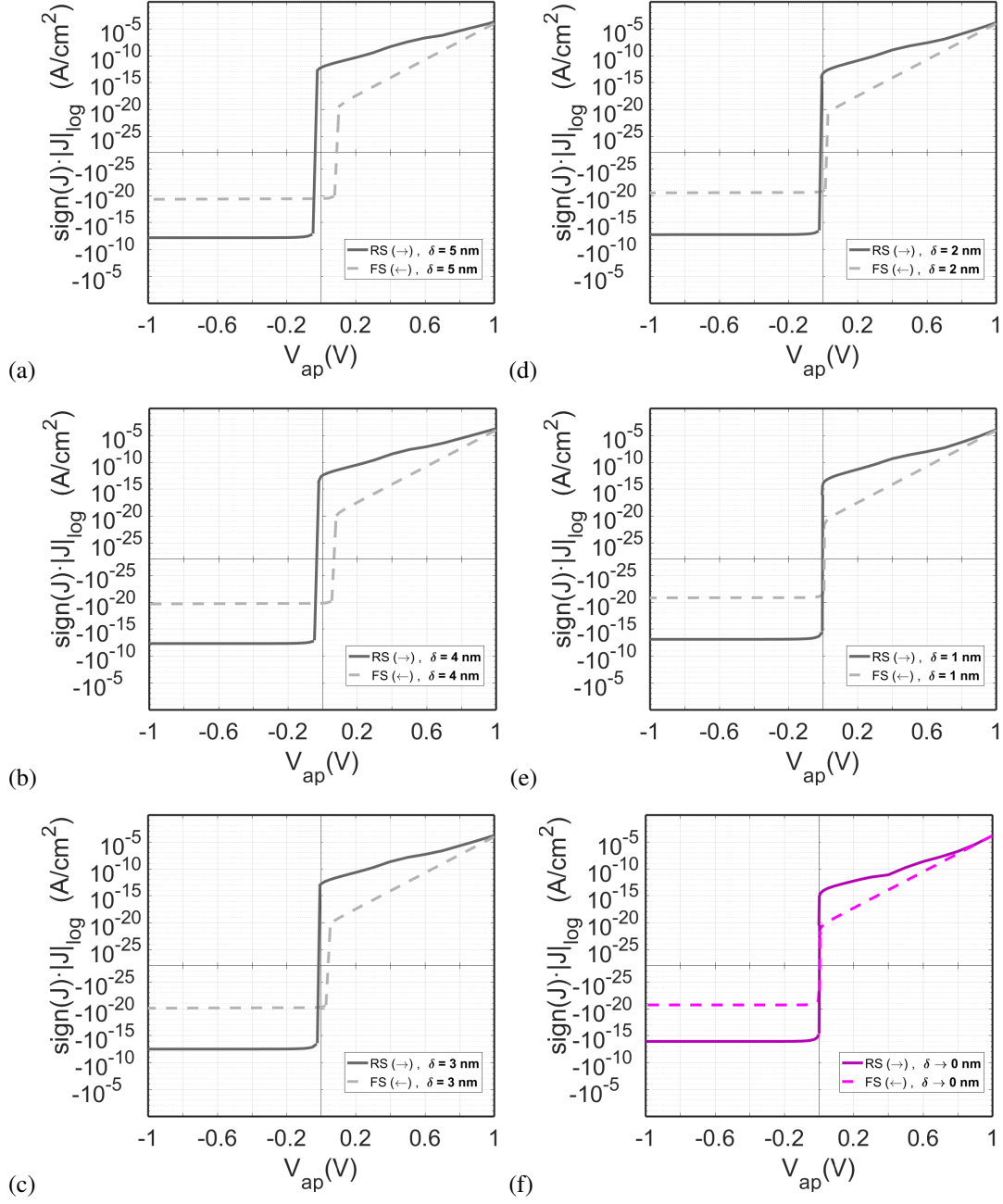


Figure S9: $J - V$ curves calculated using the interface recombination Model 4 with $N_{\text{ion}} = 5 \times 10^{17} \text{ cm}^{-3}$ and (a) $\delta = 5$ nm; (b) $\delta = 4$ nm; (c) $\delta = 3$ nm; (d) $\delta = 2$ nm; (e) $\delta = 1$ nm; and (f) limit case $\delta \rightarrow 0$ nm, evaluated using boundary conditions for the pvk/CTL interfaces (10) and (12).

Figures S10(a) and S10(b) show a linear representation of some of the cases represented above in Figs. S8 and S9, respectively. The same cases of Figs. S10(a) and S10(b) are represented in the main text in a semi-logarithmic scale in Figs. 6(a) and 6(b), respectively.

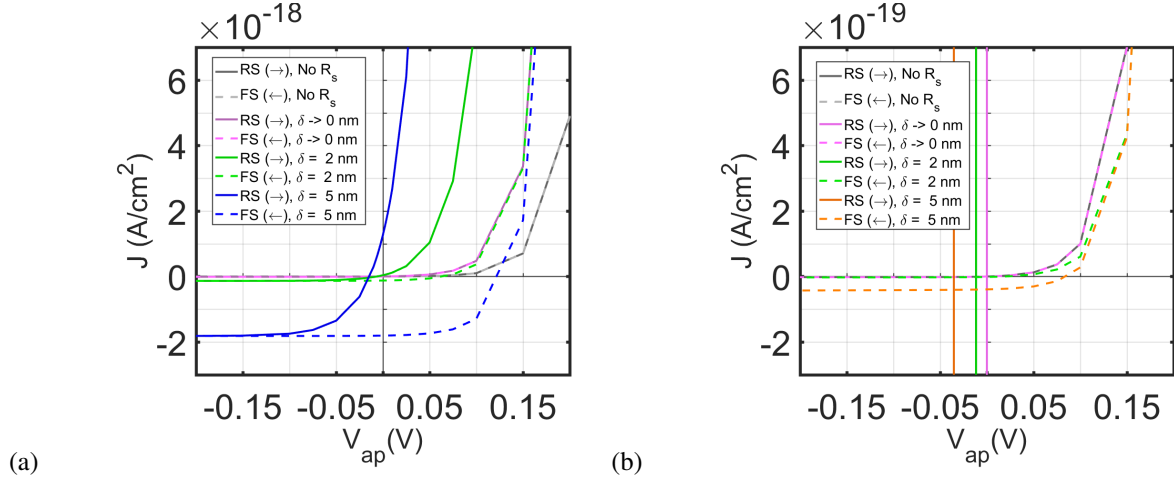


Figure S10: Fast $J - V$ curves calculated for different values of δ in the range [0, 5] nm with $N_{ion} = 5 \times 10^{17} \text{ cm}^{-3}$ and $B_S = 10^{-14} \text{ cm}^3 \text{ s}^{-1}$ using, respectively: (a) the interface recombination Model 3 (previously represented separately in Fig. S8(a)-(e)), and (b) Model 4 (previously represented separately in Fig. S9(a)-(e)). A linear scale is used here for $V_{ap} \in [-0.2, 0.2]$ V. The gray curves show the reference case with $R_S = 0$ and the same concentration of ions.

S7. Effect of the ion concentration in Models 3 and 4

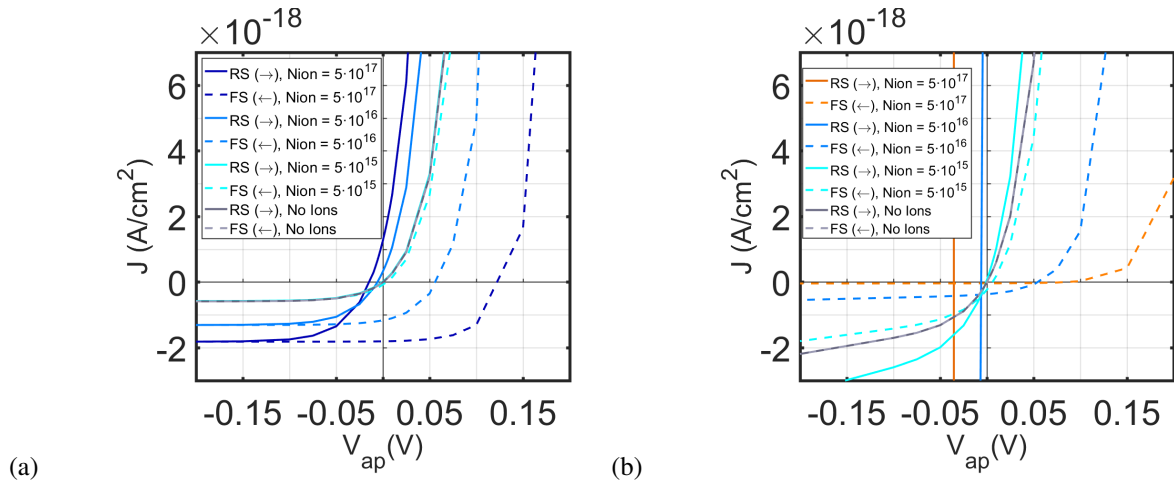


Figure S11: Linear-scale representation of fast $J - V$ curves calculated with $\delta = 5$ nm and $B_S = 10^{-14} \text{ cm}^3 \text{ s}^{-1}$ for different values of the ion concentration N_{ion} in the range $0 - 5 \times 10^{17} \text{ cm}^{-3}$, using (a) the interface recombination Model 3 and (b) the interface recombination Model 4.

S8. Effect of the built-in voltage (band alignment at the interfaces) in Models 3 and 4

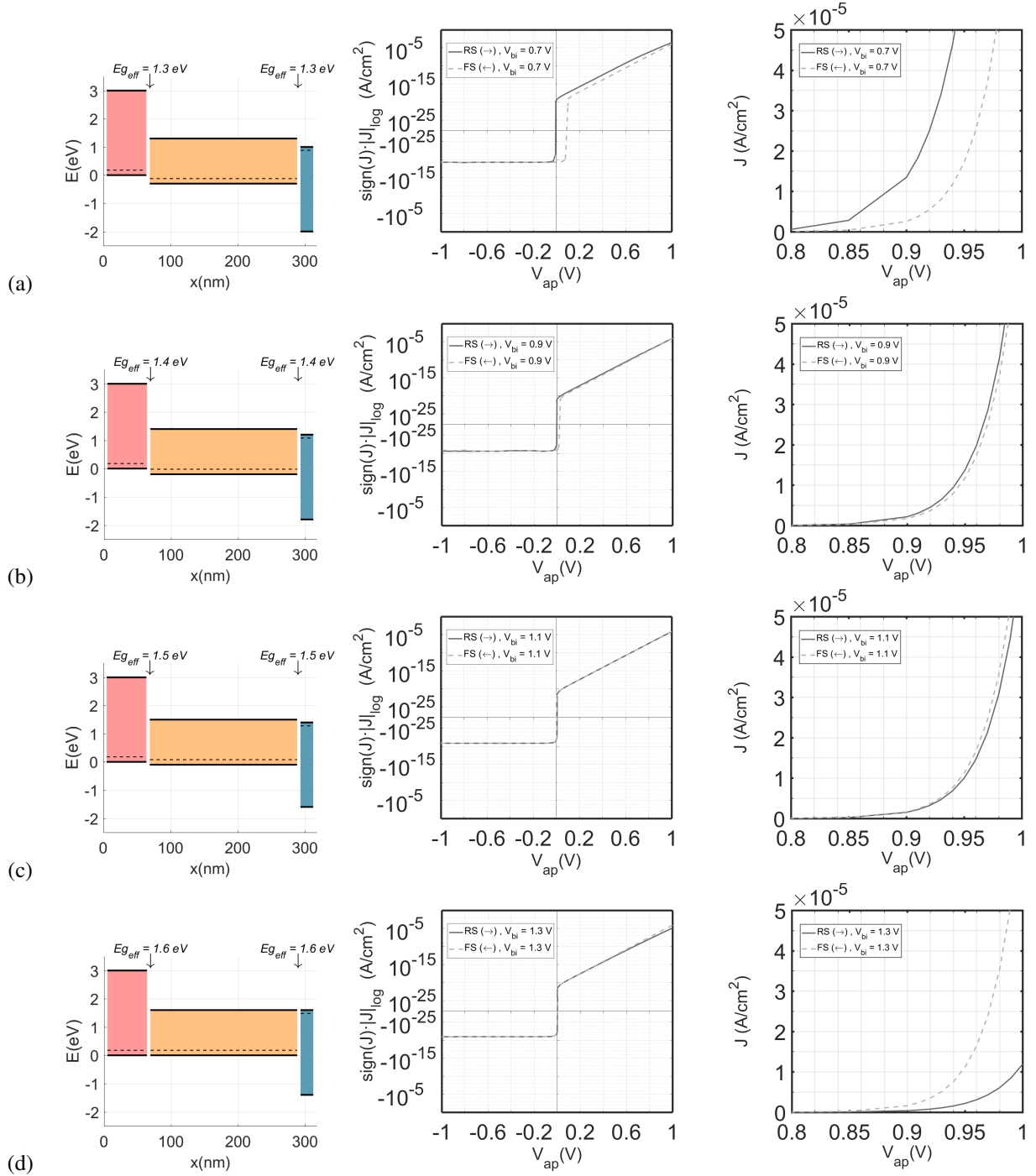


Figure S12: Fast $J - V$ curves in logarithmic scale (central column) and a in detail for $V_{ap} > 0.8$ V in linear scale (right column), calculated for different PSCs with energy diagrams (represented for the separate layers) shown in the left column. The interface recombination Model 3 is used in both interfaces ($N_{ion} = 5 \times 10^{17} \text{ cm}^{-3}$). (a) $V_{bi} = 0.7$ V ($E_{g,eff} = 1.3$ eV), (b) $V_{bi} = 0.9$ V ($E_{g,eff} = 1.4$ eV), (c) $V_{bi} = 1.1$ V ($E_{g,eff} = 1.5$ eV), (d) $V_{bi} = 1.3$ V ($E_{g,eff} = 1.6$ eV).

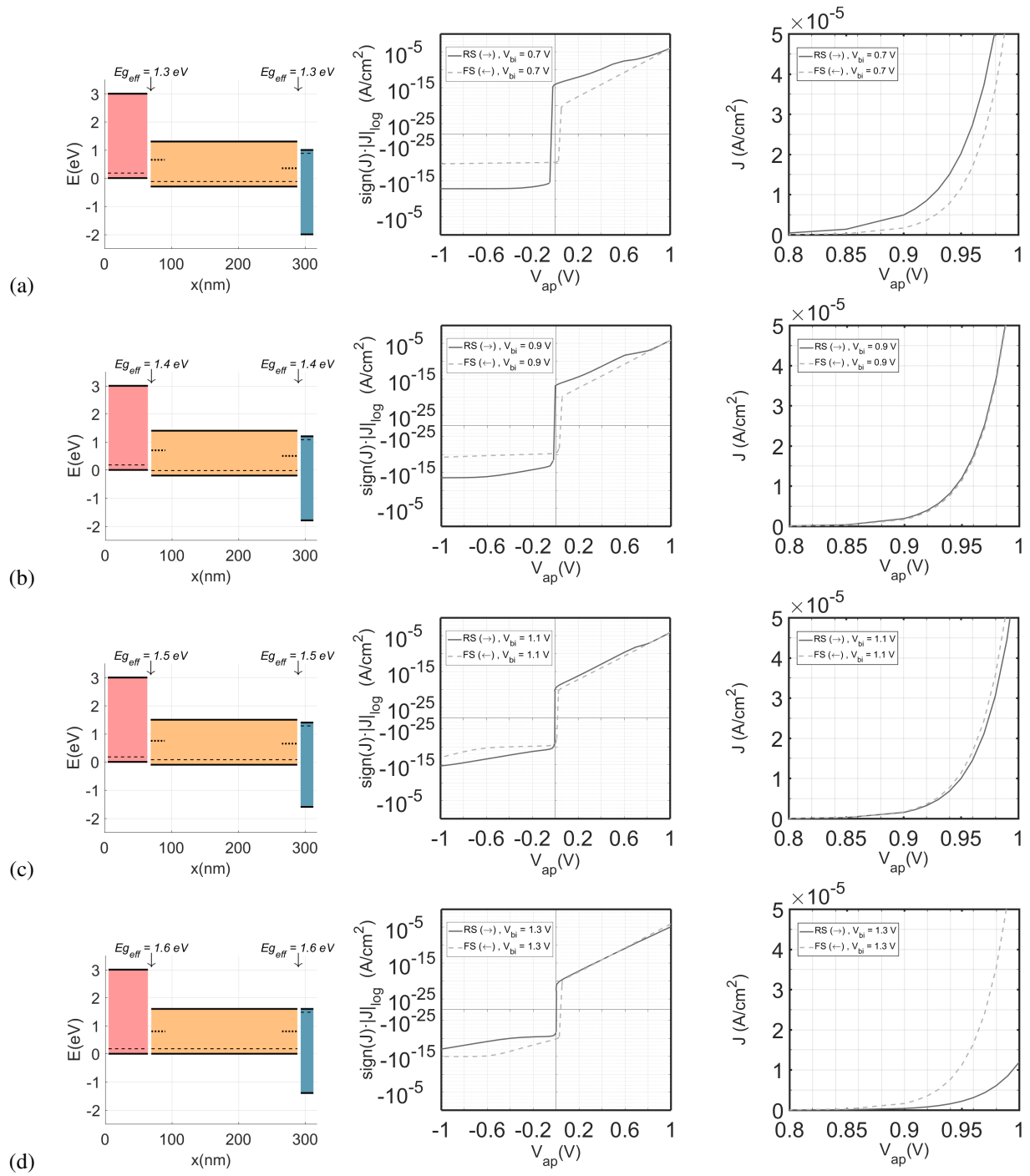


Figure S13: Fast $J - V$ curves in logarithmic scale (central column) and a in detail for $V_{ap} > 0.8$ V in linear scale (right column), calculated for different PSCs with energy diagrams (represented for the separate layers) shown in the left column. The interface recombination Model 4 is used in both interfaces ($N_{ion} = 5 \times 10^{17} \text{ cm}^{-3}$). (a) $V_{bi} = 0.7$ V ($E_{g,eff} = 1.3$ eV), (b) $V_{bi} = 0.9$ V ($E_{g,eff} = 1.4$ eV), (c) $V_{bi} = 1.1$ V ($E_{g,eff} = 1.5$ eV), (d) $V_{bi} = 1.3$ V ($E_{g,eff} = 1.6$ eV).

The center columns of Figs. S12 and S13 show the fast $J - V$ curves previously calculated, and depicted in logarithmic scale in Fig. 8, for Model 3 and Model 4. Other cases for $E_{g_{eff}}$ and V_{bi} are also analyzed and included in Figs. S12 and S13. These curves are also depicted in detail for $V_{ap} > 0.8$ V and using a linear scale (right column). The right columns in Figs. S12 and S13 show how the hysteresis first diminishes at high values of V_{ap} while $E_{g_{eff}}$ increases, changing from normal to inverted hysteresis around $E_{g_{eff}} = 1.45$ V, and later increases if $E_{g_{eff}}$ keeps rising. The current density, in both reverse and forward sweeps, diminishes when the built-in voltage increases (or $E_{g_{eff}}$ increases), but the decrease is greater in the reverse sweep. This is more clearly observed if these curves are represented in linear scale (see right column of Figs. S12 and S13). This is explained by the different distributions of ions at the beginning of each sweep, which remain constant in each one.

If the value of V_{bi} keeps increasing, making $E_{g_{eff}} > E_{g_{pvk}} = 1.6$ eV, the extraction of charge from the perovskite through the pvk/CTL interface is hindered, the reverse sweep is much lower than the forward sweep (see Figs. S14 and S15).

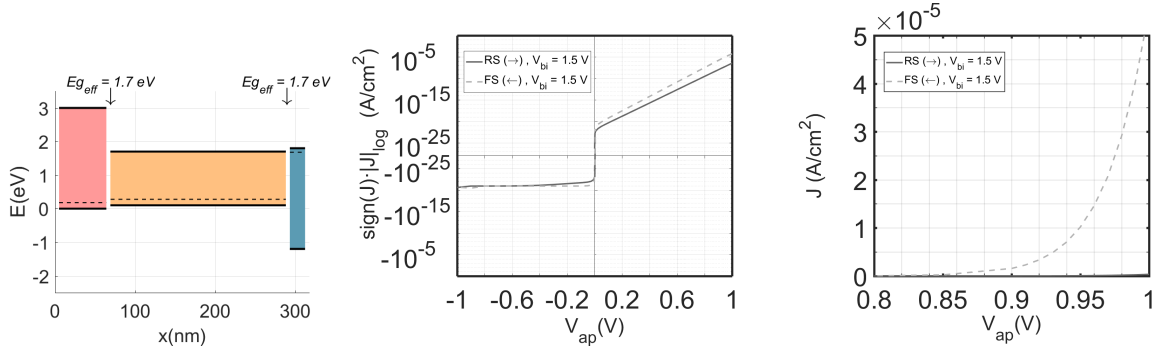


Figure S14: Fast $J - V$ curves in logarithmic scale (central column) and a detail for $V_{ap} > 0.8$ V in linear scale (right column), calculated for a PSC with energy diagrams (represented for the separate layers in equilibrium) shown in the left column. The interface recombination Model 3 is used in both interfaces, $N_{ion} = 5 \times 10^{17} \text{ cm}^{-3}$, $V_{bi} = 1.5$ V and $E_{g_{eff}} = 1.7$ eV.

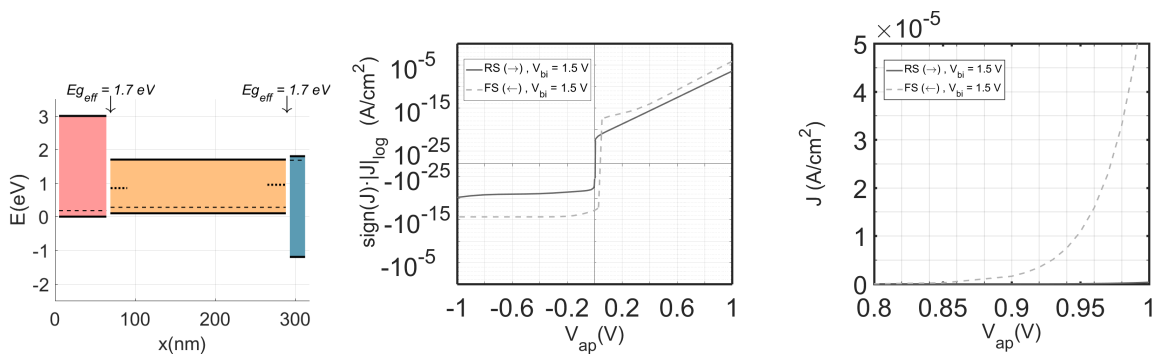


Figure S15: Fast $J - V$ curves in logarithmic scale (central column) and a detail for $V_{ap} > 0.8$ V in linear scale (right column), calculated for a PSC with energy diagrams (represented for the separate layers in equilibrium) shown in the left column. The interface recombination Model 4 is used in both interfaces, $N_{ion} = 5 \times 10^{17} \text{ cm}^{-3}$, $V_{bi} = 1.5$ V and $E_{g_{eff}} = 1.7$ eV.

S9. Effect of the shunt resistance

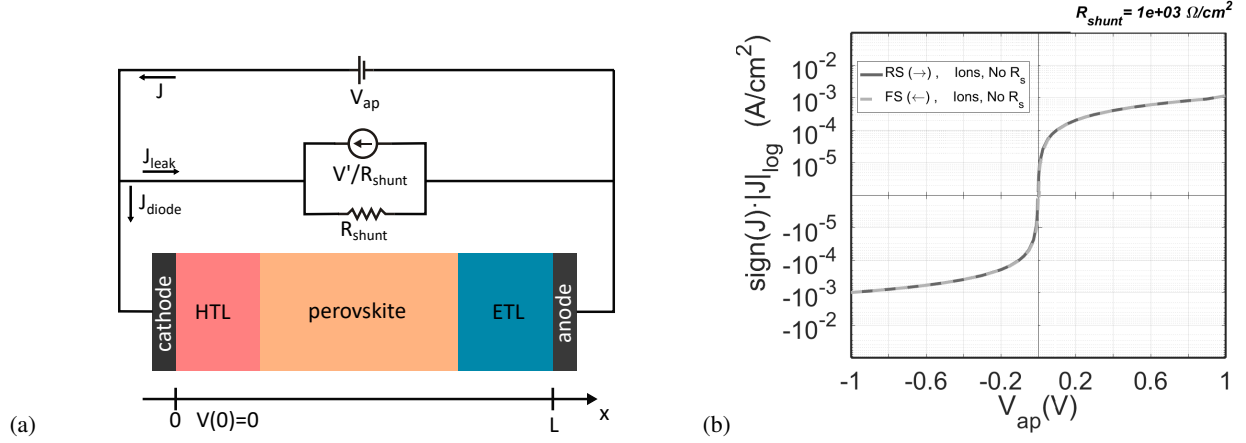


Figure S16: (a) PSC structure including current leakages in the perovskite with J_{leak} defined in (13). (b) Fast $J - V$ in darkness calculated as a reference case for comparison reasons with $N_{ion} = 5 \times 10^{17} \text{ cm}^{-3}$, no interface recombination model, and shunt resistance $R_{shunt} = 10^3 \Omega/\text{cm}^2$.

The effect of the shunt resistance is introduced in a PSC in darkness with ion concentration $N_{ion} = 5 \times 10^{17} \text{ cm}^{-3}$ inside the perovskite semiconductor, and no interface recombination in any of its interfaces. Figure S16 shows the fast $J - V$ in darkness calculated for this reference case.

Now, the effect of the shunt resistance is studied on the cases analyzed in Fig. 4: a PSC in dark conditions with ion concentration $N_{ion} = 5 \times 10^{17} \text{ cm}^{-3}$ inside the perovskite semiconductor, and the interface recombination Models 1 (4), 2 (6), 3 (7) and 4 (9) applied in both interfaces. Adding the effect of a shunt resistance $R_{shunt} = 10^3 \Omega\cdot\text{cm}^2$, the resulting new $J - V$ curves can be seen in Figs. S17a, S17b, S17c and S17d, respectively. Figures S17c and S17d are Figs. 10a and 10b in the main text, reproduced here for comparison purposes.

The small hysteresis loops shown in Figs. 4a-4b are undetected in the respective Figs. Figs. S17a- S17b, hidden by the leakage current.

Figs. S17a and S17c, for Models 1 and 3, respectively, show a change in the slope at $V_{ap} > 0.9 \text{ V}$. Figure S18 shows the $J - V$ curve of Fig. S17c decomposed into J_{leak} and J_{diode} , confirming this fact.

The change is greater in the reverse sweep than in the forward one (i.e. $(dJ/dV_{ap})_{RF} > (dJ/dV_{ap})_{FR}$). This increment is due to the fact that the diode current J_{diode} surpasses the value of the leakage current J_{leak} . Figures S18a-S18b show these two components, J_{diode} and J_{leak} , of the $J - V$ curve represented in Fig. S17c, and the value of V_{ap} at which the values of these two components coincide: $V_{ap} < 1 \text{ V}$ in the reverse sweep represented in Fig. S18a, and $V_{ap} > 1 \text{ V}$ in the forward sweep represented in Fig. S18b. In this last case the crossing is out of the represented range.

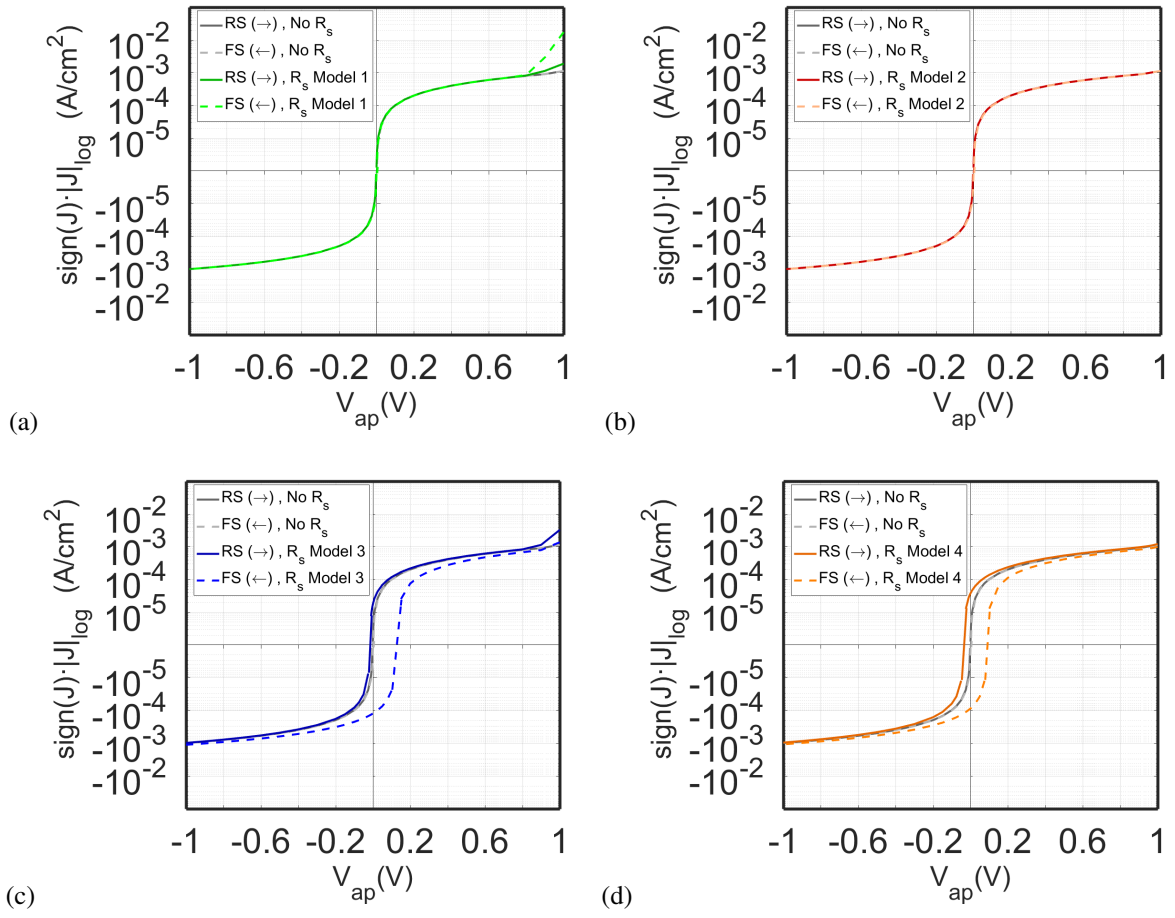


Figure S17: Fast $J - V$ curves in dark conditions calculated with $N_{ion} = 5 \times 10^{17} \text{ cm}^{-3}$, a shunt resistance $R_{shunt} = 10^3 \text{ } \Omega \cdot \text{cm}^2$ and using (a) Model 1 with $B_S = 10^{-6} \text{ cm}^3 \text{ s}^{-1}$; (b) Model 2 with $(\tau_n = \tau_p = 1 \text{ ms})$; (c) Model 3 with $B_S = 10^{-14} \text{ cm}^3 \text{ s}^{-1}$; and (d) Model 4 with $\tau_n = \tau_p = 1 \text{ ms}$.

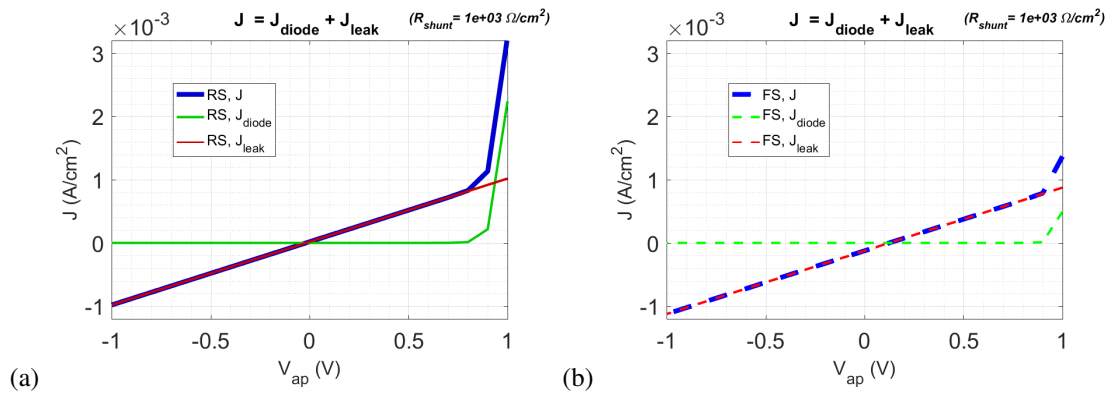


Figure S18: J_{diode} and J_{leak} components corresponding to the case represented in Fig. S17c. (a) reverse sweep and (b) forward sweep.